

Electrodynamics of a prototypical altermagnetic compound MnTe

Bixia Gao(高碧霞), Yixuan Luo(罗伊轩), Liye Cao(曹立叶), Tao Sun(孙涛), Zehao Yu(于泽浩), Lei Wang(王蕾), Xinyu Zhang(张新雨), Hongbo Hu(胡宏波), Yanfeng Guo(郭艳峰), and Rongyan Chen(陈荣艳)

Citation: Chin. Phys. B, 2026, 35 (**3**): 037801. DOI: 10.1088/1674-1056/ae2abc
http://cpb.iphy.ac.cn; http://iopscience.iop.org/cpb

What follows is a list of articles you may be interested in

Effects of helium ion irradiation and thermal annealing on the optical and structural properties of hexagonal boron nitride

Guan-Lin Liu(刘冠麟), Ji-Lian Xu(徐辑廉), Peng-Tao Jing(景鹏涛), Jing-Jing Shao(邵京京), Xu Guo(郭旭), Yun-Tao Wu(吴韵涛), Feng Qin(覃凤), Zhen Cheng(程祯), Deming Liu(刘德明), Yang Bao(鲍洋), Hai Xu(徐海), Li-Gong Zhang(张立功), Da Zhan(詹达), Jia-Xu Yan(闫家旭), Lei Liu(刘雷), and De-Zhen Shen(申德振)

Chin. Phys. B, 2025, 34 (**5**): 057801. DOI: 10.1088/1674-1056/adbee7

Optical study of magnetic topological insulator $MnBi_4Te_7$

Zhi-Yu Liao(廖知裕), Bing Shen(沈冰), Xiang-Gang Qiu(邱祥冈), and Bing Xu(许兵)

Chin. Phys. B, 2024, 33 (**1**): 017802. DOI: 10.1088/1674-1056/ad08aa

Effect of heating time on structural, morphology, optical, and photocatalytic properties of g-C_3N_4 nanosheets

Nguyen Manh Hung, Le Thi Mai Oanh, Lam Thi Hang, Pham Do Chung, Pham Thi Duyen, Dao Viet Thang, Nguyen Van Minh

Chin. Phys. B, 2020, 29 (**5**): 057801. DOI: 10.1088/1674-1056/ab7e95

Optical investigation of topological semimetal $SrMnSb_2$

Zi-Yang Qiu(邱子阳), Zhi-Yu Liao(廖知裕), Xiang-Gang Qiu(邱祥冈)

Chin. Phys. B, 2019, 28 (**4**): 047801. DOI: 10.1088/1674-1056/28/4/047801

Magnetic field aligned orderly arrangement of Fe_3O_4 nanoparticles in CS/PVA/Fe_3O_4 membranes

Meng Du(杜萌), Xing-Zhong Cao(曹兴忠), Rui Xia(夏锐), Zhong-Po Zhou(周忠坡), Shuo-Xue Jin(靳硕学), Bao-Yi Wang(王宝义)

Chin. Phys. B, 2018, 27 (**2**): 027805. DOI: 10.1088/1674-1056/27/2/027805

RAPID COMMUNICATION

Electrodynamics of a prototypical altermagnetic compound MnTe

Bixia Gao(高碧霞)[1,2], Yixuan Luo(罗伊轩)[3], Liye Cao(曹立叶)[1,2], Tao Sun(孙涛)[4], Zehao Yu(于泽浩)[1,2], Lei Wang(王蕾)[1,2], Xinyu Zhang(张新雨)[1,2], Hongbo Hu(胡宏波)[1,2], Yanfeng Guo(郭艳峰)[3,5], and Rongyan Chen(陈荣艳)[1,2,†]

[1] *Center for Advanced Quantum Studies, School of Physics and Astronomy, Beijing Normal University, Beijing* 100875, *China*
[2] *Key Laboratory of Multiscale Spin Physics, Ministry of Education, Beijing Normal University, Beijing* 100875, *China*
[3] *State Key Laboratory of Quantum Functional Materials, School of Physical Science and Technology, ShanghaiTech University, Shanghai* 201210, *China*
[4] *Beijing National Laboratory for Condensed Matter Physics, Institute of Physics, Chinese Academy of Sciences, Beijing* 100190, *China*
[5] *ShanghaiTech Laboratory for Topological Physics, ShanghaiTech University, Shanghai* 201210, *China*

(Received 1 September 2025; revised manuscript received 5 December 2025; accepted manuscript online 10 December 2025)

Altermagnetism, characterized by compensated antiparallel spins and momentum-dependent spin splitting, has offered a promising platform for novel spintronic phenomena. Among this class of materials, hexagonal MnTe stands out due to its high Néel temperature and giant spin splitting. However, a comprehensive understanding of its charge dynamics remains incomplete. Here, we employ infrared spectroscopy to investigate the charge dynamics of single crystalline MnTe. The low energy optical conductivity reveals a suppressed Drude response across all temperatures, consistent with the reported p-type doping as indicated by previous angle-resolved photoemission spectroscopy (ARPES) measurement. An indirect band gap of about 0.48 eV attributed to impurity-assisted transitions, and a direct gap of 1.60 eV are identified via the Tauc relation at 10 K. Moreover, we observe a subtle difference at around 1.44 eV in the optical conductivity between the antiferromagnetic and paramagnetic states, which might be linked to altermagnetism-related band splitting. Additionally, Fano line shape analysis of a phonon mode at around 135 cm^{-1} reveals appreciable coupling between the phonon and spin fluctuations near the Néel temperature. Our results provide key insights into the charge dynamics of MnTe, underscoring its rich physics beyond a conventional semiconductor.

Keywords: altermagnetism, MnTe, infrared spectroscopy

PACS: 78.30.–j, 78.40.Fy, 63.20.–e, 75.50.Ee

DOI: 10.1088/1674-1056/ae2abc **CSTR:** 32038.14.CPB.ae2abc

1. Introduction

Altermagnetism has drawn a great deal of attention recently as a novel magnetic state that diverges from traditional ferromagnetism and antiferromagnetism.[1–3] In this intriguing phenomenon, spins are ordered collinearly with antiparallel alignment, akin to antiferromagnets, yet the electronic structure exhibits time-reversal symmetry breaking through momentum-dependent spin splitting.[1,2] Unlike conventional ferromagnets, altermagnets lack net magnetization, but their spin-polarized bands enable exotic quantum phenomena such as the anomalous Hall effect (AHE), spin-splitter torque, nonrelativistic magneto-optical responses, and so on.[4–8] This unique interplay of compensated magnetism and spin momentum locking positions altermagnets as a promising platform for high-speed spintronic devices and fundamental studies of symmetry breaking mechanisms.

Among the growing family of altermagnetic candidates, α-MnTe with a hexagonal NiAs-type lattice structure (space group $P6_3/mmc$) stands out due to its robust collinear antiferromagnetic (AFM) order with a high Néel temperature of about 310 K and giant spin splitting exceeding 300 meV.[2,9–16] Its crystal structure consists of ferromagnetically aligned Mn layers stacked antiferromagnetically along the c-axis, while nonmagnetic Te atoms occupy octahedral sites, breaking inversion symmetry between spin sublattices.[16,17] This structural asymmetry, combined with strong p–d orbital hybridization, generates a spin-split electronic structure, as revealed by ARPES.[16] Recent experiments further demonstrate spontaneous AHE in MnTe thin films,[18] providing direct evidence of time-reversal symmetry breaking due to altermagnetic order. Theoretical studies suggest that this behavior originates from anisotropic superexchange interactions and relativistic spin–orbit coupling, which collectively stabilize the alternating spin polarization in momentum space.[18]

Despite significant progress in understanding the altermagnetic properties of MnTe, critical questions regarding its charge dynamics remain unresolved. Previous studies have reported both direct and indirect band gaps, with energies varying from 0.21 eV to 1.35 eV.[19–28] Moreover, in an altermagnetic compound such as MnTe, the predicted spin-split bands may give rise to distinct optical transitions between the spin-

†Corresponding author. E-mail: rychen@bnu.edu.cn

© 2026 Chinese Physical Society and IOP Publishing Ltd. All rights, including for text and data mining, AI training, and similar technologies, are reserved.

polarized states. To investigate these features, we employ Fourier-transform infrared spectroscopy to study the charge dynamics of single crystalline MnTe. Our measurements reveal an indirect gap of 0.475 eV, along with a direct gap of 1.60 eV at 10 K. Furthermore, a detailed line shape analysis of the optical conductivity reveals weak but discernible features that we associate with the anticipated spin-splitting of the bands.

2. Experimental details

MnTe single crystals were grown via the flux method. The starting materials, consisting of Mn plates (99.9%, Macklin), Te powders (99.99%, Macklin), and Sb blocks (99.999%, Macklin), were mixed in a molar ratio of 1:1:20 and loaded into an alumina crucible. The crucible was then sealed under vacuum in a quartz tube. The assembly was heated in a furnace to 1050 °C over 15 hours, held at this temperature for 10 hours, and subsequently cooled slowly to 700 °C at a rate of 2 °C/h. At this temperature, the excess Sb flux was removed using a high-speed centrifuge. Finally, black shiny crystals with typical dimensions of $5\times4\times1$ mm^3 were obtained. The x-ray diffraction (XRD) pattern was obtained using a Rigaku SmartLab diffractometer with Cu $K\alpha$ radiation in Bragg–Brentano (θ–2θ) geometry. The temperature-dependent resistivity was measured using the standard four-probe method in a physical property measurement system, with the current flowing along the *ab* plane. The optical reflectivity measurement was performed on a Bruker Vertex 80 V spectrometer in the frequency range 40–22000 cm^{-1}. In order to obtain the exact reflectivity $R(\omega)$ value, we use a technology of *in situ* coating of a gold or aluminum film on the sample. The real part of the optical conductivity $\sigma_1(\omega)$, together with the refractive index n and extinction coefficient k, is obtained by applying a Kramers–Kronig (KK) transformation to the measured reflectivity $R(\omega)$. For the KK analysis, we use the Hagen–Rubens relationship to extrapolate in the low-frequency part of $R(\omega)$, and we use the x-ray atomic diffraction function to extrapolate in the high-frequency part.[29]

3. Results and discussion

To verify the crystal structure of the MnTe single crystals used for infrared spectroscopy, we conduct a room-temperature XRD measurement. As shown in Fig. 1(a), the θ–2θ scans display only the (00l) reflections with $l = 2, 4, 6$ of hexagonal NiAs-type MnTe ($P6_3/mmc$). The peak positions agree with previously reported values[30,31] and no impurity peaks are observed within the accuracy of the measurement. The result confirms that our MnTe single crystals are in the α-phase and exhibit high quality.

The temperature-dependent resistivity $\rho(T)$ of our MnTe sample is shown in Fig. 1(b). The data reveal a complex non-monotonic evolution, suggesting the interplay of several scattering mechanisms across different temperature regimes. Upon cooling from 350 K, $\rho(T)$ remains nearly constant within a narrow temperature window before undergoing a sharp decrease around 300 K. This downward trend persists until approximately 100 K, below which $\rho(T)$ begins to increase monotonically down to the lowest measured temperature. To elucidate these features more clearly, we have calculated the derivative of $\rho(T)$, as presented in the lower inset of Fig. 1(b). A pronounced peak appears at $T_N = 305$ K, corresponding to the AFM phase transition temperature, which is close to previous reports (e.g., 307 K or 310 K[2,9–16]). Additionally, the derivative of $\rho(T)$ changes sign at 85 K, demarcating two distinct regimes in the resistivity behavior.

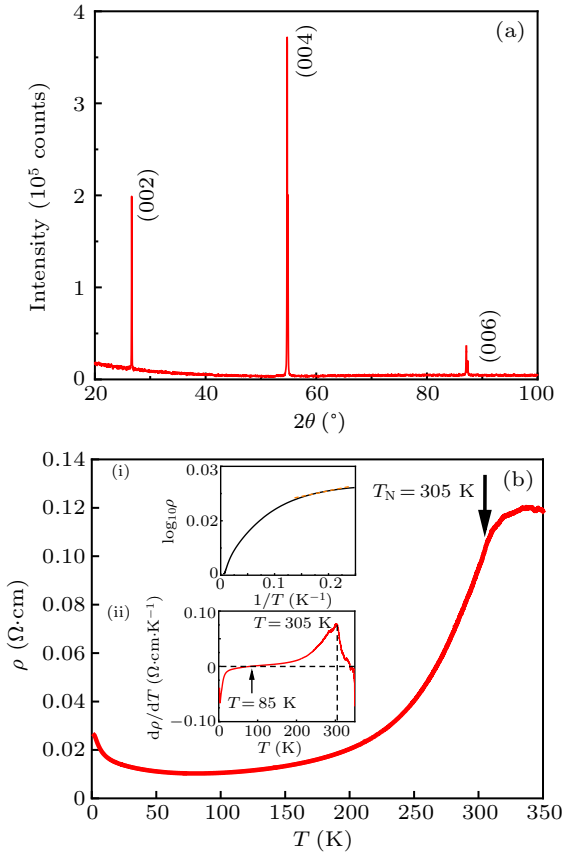


Fig. 1. (a) XRD pattern of single crystal MnTe at room temperature. (b) The temperature-dependent *ab*-plane resistivity $\rho(T)$ of bulk MnTe. The red line indicates the cooling process. The inset (i) displays the Arrhenius plot of MnTe resistivity measured from 2.1 K to 85 K. The orange dashed line represents linear fits based on the activated hopping formula $\rho = \rho_0 \exp[E_g/k_B T]$. The inset (ii) presents $d\rho(T)/dT$ of MnTe as a function of temperature between 2 K and 350 K.

The increase in resistivity with decreasing temperature below 85 K is characteristic of semiconductor or insulating behaviors, consistent with the electronic property of MnTe as a semiconductor.[16,19,21–23,27,28] To further elucidate the charge transport mechanism in the low temperature regime, the $\rho(T)$ from 2 K to 85 K was analyzed using an Arrhenius plot, where $\log_{10}\rho(T)$ is plotted against $1/T$, as shown in the upper inset of Fig. 1(b). This approach is based on the thermally acti-

vated relation $\rho = \rho_0 \exp[E_g/k_B T]$ for semiconductors or insulators, and a linear relationship is expected in this plot. Nevertheless, we observe a continuously varying slope across this temperature range. This deviation suggests the involvement of multiple conduction processes, such as hopping transport and impurity-assisted conduction. A linear fitting in the very low temperature range of 2.1–3.3 K yields an activation energy of $E_g = 1.94 \times 10^{-3}$ eV, as indicated by the orange dashed line in the upper inset of Fig. 1(b). The magnitude of the obtained E_g is consistent with the impurity activation energy reported by Pereverzev *et al.*[32] Above 85 K, $\rho(T)$ increases upon warming, suggesting contributions from optical phonon scattering[32] and the magnon-drag effects,[33] both of which intensify at higher temperatures. Above T_N, the long-range spin order is destroyed, and conduction electrons are scattered by disordered spins, causing the resistivity to remain nearly constant at a high value.

Figure 2 displays the in-plane reflectivity $R(\omega)$ of MnTe up to 22000 cm^{-1} at several selected temperatures. Unlike typical semiconductors,[34,35] MnTe exhibits a pronounced temperature dependence in a large energy window. Below T_N, the low-frequency $R(\omega)$ increases significantly upon cooling, and it exhibits a pronounced rise with decreasing frequency below 100 cm^{-1} at low temperatures, both of which are hallmarks of metallic behavior. Concurrently, a sharp peak–dip structure could be clearly observed above 200 K, characteristic of phonon features typically observed in the reflectivity spectra of semiconductors or insulators. However, the dip structure gradually diminishes with decreasing temperature, suggesting the screening effect related to conduction electrons.[35,36] This evolution further demonstrates the existence of free carriers in MnTe, although it is a reported semiconductor.[16,19,21–23,27,28] In other words, MnTe is a doped semiconductor. Our results are consistent with previous ARPES measurements, which reveal hole-like bands near the Fermi level,[16,37] indicating p-type doping in this compound.

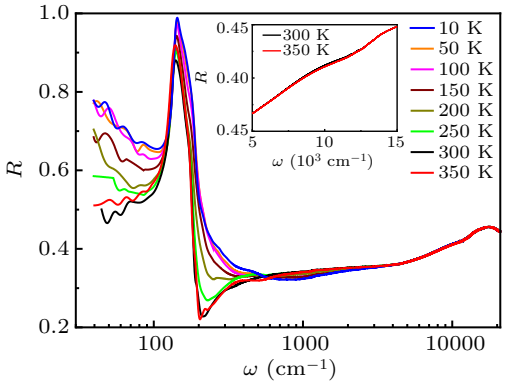


Fig. 2. The temperature-dependent optical reflectivity $R(\omega)$ for MnTe below 22000 cm^{-1}. The inset provides a detailed view of $R(\omega)$ at 300 K and 350 K within the spectral range of 5000–15000 cm^{-1}.

The reflectivity at 350 K deviates from the evolution trend observed below T_N, as the low-frequency component (< 100 cm^{-1}) is obviously higher than that at 300 K. Furthermore, although reflectivity spectra below T_N converge above ~ 4000 cm^{-1} within experimental uncertainty, a subtle difference emerges between 300 K and 350 K in the 6800–12600 cm^{-1} range, as highlighted in the inset of Fig. 2. To confirm the reproducibility of this feature, we have conducted repeated measurements at 250 K, 300 K, and 350 K. It is found that the spectra at 250 K and 300 K are always identical, whereas a consistent difference persists between 300 K and 350 K. These observations demonstrate that the electronic structure is somewhat modified by the AFM order, which will be discussed in more detail in the following analysis of the optical conductivity $\sigma_1(\omega)$.

The obtained optical conductivity $\sigma_1(\omega)$ at various temperatures is shown in Fig. 3(a). The low energy responses well below the absorption edge are shown in the inset of Fig. 3(a). $\sigma_1(\omega)$ displays a Drude-like response, typically associated with metallic systems. This feature, characterized by a peak centered at zero frequency with a width governed by the carrier scattering rate γ, indicates the presence of itinerant charge carriers. However, unlike conventional metals that exhibit a strong and sharp Drude peak, MnTe shows a markedly suppressed low-frequency conductivity, in agreement with its semiconducting nature and low direct-current conductivity. Therefore, the presence of itinerant carriers is consistent with the p-type doping as revealed by ARPES experiments.[16,37] As the temperature increases, the Drude peak broadens, indicating an increase in the scattering rate. The carrier density N could be estimated by the plasma frequency ω_p, which is linked to carrier density via $\omega_p^2 = \frac{4\pi N_e^2}{m^*}$. The plasma frequency ω_p was estimated using the formula $\omega_p^2 = \frac{120}{\pi\Omega^{-1}} \int_0^{\omega_c} \sigma_1(\omega)\,\mathrm{d}\omega$, where ω_c represents a cutoff frequency that encompasses all intraband transitions while excluding interband transitions. We obtained $\omega_p^2 = 6.30 \times 10^5$ cm^{-2} at 10 K using the cutoff frequency of $\omega_c = 1200$ cm^{-1}, yielding the carrier density N to be approximately 2.94×10^{19} cm^{-3}, in good agreement with the values obtained from other experimental techniques.[15]

Unlike the sharp absorption edges of the real part of optical conductivity in typical semiconductors, that of MnTe extends continuously from 5000 cm^{-1} to 17000 cm^{-1}, suggesting a complex interband transition scheme. To unravel the underlying mechanism, we analyzed this edge using the Tauc relation:[38,39]

$$(\varepsilon_2 \omega^2)^n \propto \hbar\omega - E_g, \tag{1}$$

where ε_2 is the imaginary part of the dielectric function, and E_g is the optical band gap. The exponent n specifies the type of transition: $n = 2$ for direct allowed transitions and $n = 1/2$ for indirect ones. The nature of the gap can be identified by which exponent yields a distinct linear region in the Tauc plot. The optical gap energy E_g is then determined by extrapolating

the linear fit of this region to the energy axis. As shown in Fig. 3(b), the Tauc plot at 10 K for $n = 1/2$ (red solid line, left axis) exhibits two distinct linear segments, each fitted by a red dashed line. This behavior is characteristic of an indirect gap. The extrapolated energies from these two fits are 0.20 eV and 0.75 eV, as marked by black arrows in Fig. 3(b), which correspond to $E_g \pm E_{as}$, where E_{as} represents the energy of the assistant involved in the indirect transition. This yields an actual indirect band gap energy of 0.475±0.275 eV.

Given the nature of the indirect gap, phonons are typically expected to assist the interband transitions. However, since the phonon population is highly temperature-dependent while the absorption edge shows little temperature dependence, it is unlikely that phonons play a major role in this process. Furthermore, the indirect gap energy obtained here (0.475 eV) is significantly smaller than previously reported values (∼ 1.27 eV[27,28]). Considering this discrepancy and the temperature-independent behavior, we infer that impurities most likely assist the indirect transitions in our sample. This inference is consistent with our transport measurement results. Notably, although our data strongly suggest an impurity-assisted process, a definitive distinction between phonon- and impurity-assisted transitions would require further investigations, such as temperature-dependent photoluminescence or modulation spectroscopy, which remain to be explored in future work. Furthermore, a single linear region is present in the Tauc plot for $n = 2$ (blue solid line, right axis), indicative of a direct gap. The extrapolation of its linear fit (blue dashed line) to the energy axis indicates a value of 1.60 eV at 10 K, as indicated by a black arrow in Fig. 3(b).

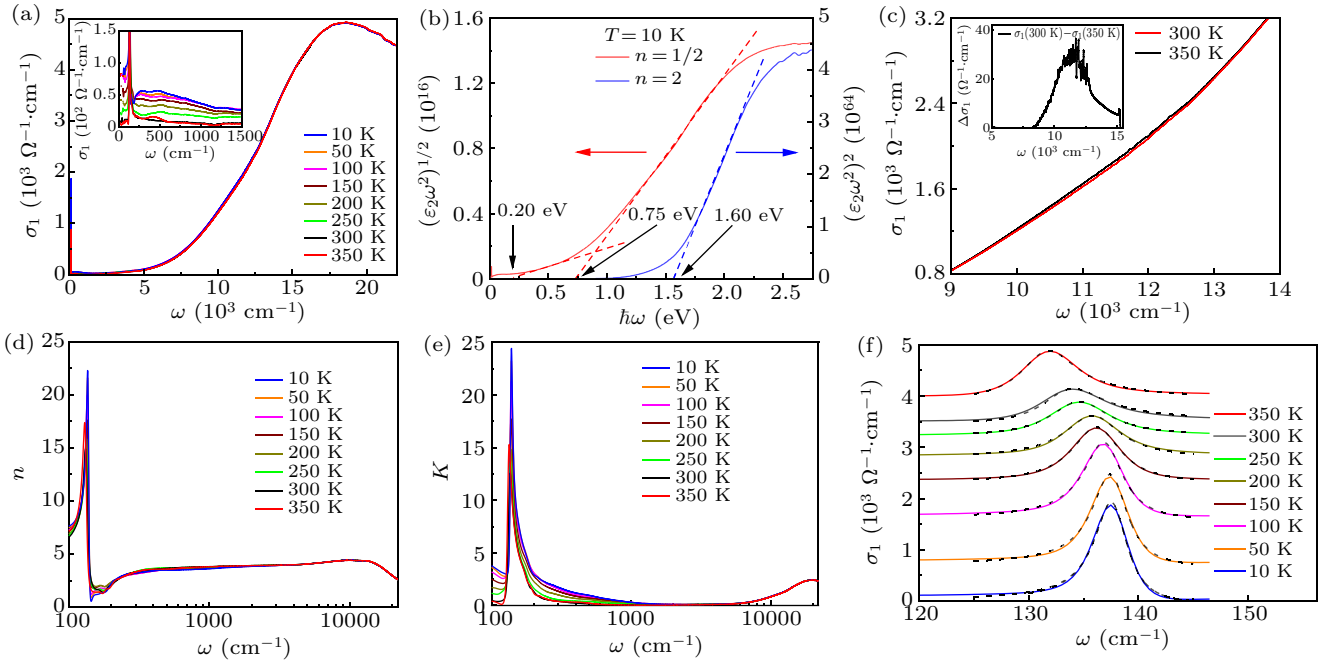


Fig. 3. (a) Real part of the optical conductivity $\sigma_1(\omega)$ of MnTe below 22000 cm^{-1} at selected temperatures. The inset displays $\sigma_1(\omega)$ in an expanded energy range up to 1500 cm^{-1}. The colored dotted lines represent the low-frequency extrapolations used in the KK transformation at different temperatures. (b) Tauc plots of MnTe at 10 K, where the red solid line corresponds to $(\varepsilon_2\omega^2)^{1/2}$ and the blue solid line corresponds to $(\varepsilon_2\omega^2)^2$; the linear regions are highlighted by dashed lines, with extrapolations to the photon-energy axis used to estimate the band gap (left y-axis: $(\varepsilon_2\omega^2)^{1/2}$, right y-axis: $(\varepsilon_2\omega^2)^2$). (c) The temperature-dependent $\sigma_1(\omega)$ of MnTe in the range of 9000 cm^{-1} to 14000 cm^{-1} at 300 K and 350 K. The inset displays the differential conductivity $\Delta\sigma_1(\omega)$ in thg range of 5000 cm^{-1} to 15000 cm^{-1} between 300 K and 350 K, i.e., $\Delta\sigma_1 = \sigma_1(300\ \mathrm{K}) - \sigma_1(350\ \mathrm{K})$. (d) Refractive index n and (e) extinction coefficient k of MnTe below 22000 cm^{-1} at selected temperatures. (f) The phonon peak of $\sigma_1(\omega)$ in the range of 120–147 cm^{-1}, and the spectra are vertically offset by temperature for clarity. The black dashed lines represent the fitting curve between 125–145 cm^{-1} at each temperature, with fitting parameters summarized in Table 1.

Notably, we found that the indirect and direct gap values are essentially temperature-independent from 10 K to 300 K, which is consistent with the almost constant absorption edge in this temperature range. This overall temperature independence is expected, as the gap energies (0.475 eV and 1.60 eV) are significantly larger than the relevant thermal energy scale (∼ 0.03 eV between 10 K and 300 K), making thermal effects too weak to induce a measurable shift. In contrast, the extracted direct and indirect gaps at 350 K are 0.51 eV and 1.58 eV, respectively, showing a slight deviation from the values below T_N. We attribute this minor change to the influence of the AFM phase transition.

To elucidate the impact of AFM order on the electronic and optical properties of MnTe, we performed a comparative analysis of $\sigma_1(\omega)$ at 300 K and 350 K. As shown in Fig. 3(c), a subtle discrepancy of $\sigma_1(\omega)$ appears in the 10000–13000 cm^{-1} at these two temperatures. This feature correlates with an analogous discrepancy in the reflectivity spectra. To highlight it more clearly, we have performed the subtraction $\Delta\sigma_1 = \sigma_1(300\ \mathrm{K}) - \sigma_1(350\ \mathrm{K})$, as displayed in the in-

set of Fig. 3(c). The differential spectrum reveals a distinct peak centered at approximately 11560 cm^{-1} (1.44 eV). We can rule out thermal broadening as its origin for two key reasons: first, the energy of this feature is significantly larger than the thermal energy scale of the measured temperature difference; second, it emerges specifically across the phase transitions (between 300 K and 350 K) and is absent in temperature variations well below T_N where thermal effects are also present. Instead, this feature may be linked to the altermagnetic phase transition. ARPES measurements[16] and theoretical calculations[18] have established that the most prominent change across T_N is a characteristic band splitting induced by the altermagnetism. We therefore propose that the observed differential peak is a manifestation of this altermagnetic splitting. Specifically, this feature possibly corresponds to interband transitions associated with electronic bands that are degenerate above T_N, but which split into separate transitions below T_N, giving rise to the differential signal. This mechanism is reminiscent of spin-driven band reconstructions in magnetically doped topological insulators such as Cr-doped Bi_2Te_3.[40] The consistency between our $\sigma_1(\omega)$ results and previous ARPES studies[16] confirms that the altermagnetic phase transition in MnTe plays a decisive role in reshaping its electronic structure. To provide a useful reference for future optical studies, we also present the refractive index n and extinction coefficient k of MnTe, which together constitute the complex index of refraction $\tilde{n} = n + ik$. The corresponding n and k below 22000 cm^{-1} at selected temperatures are shown in Figs. 3(d) and 3(e), respectively.

In addition to the absorption edge, the optical conductivity spectrum $\sigma_1(\omega)$ exhibits very sharp phonon peaks in the low energy range, as can be seen in both the main panel and inset of Fig. 3(a). To better demonstrate the phonon-related features, we present $\sigma_1(\omega)$ in the energy range 120–147 cm^{-1} in Fig. 3(f), with the spectra vertically offset by temperature for clarity. Well-defined phonon peaks are observed throughout the entire temperature range. While the peak frequency exhibits a monotonic softening upon warming, a sudden shift could be observed between 300 K and 350 K. Furthermore, all phonon peaks exhibit a slight asymmetry in their line shape. To account for this asymmetry, we perform Fano line shape fits to the phonon peaks within the 125–145 cm^{-1} range using the following expression:[41,42]

$$\sigma_1(\omega) = \frac{\sigma_0 \omega \gamma [\gamma\omega(q^2-1) + 2q(\omega^2-\omega_0^2)]}{4\pi[(\omega^2-\omega_0^2)^2 + \gamma^2\omega^2]}, \quad (2)$$

where ω_0, σ_0, and γ correspond to the resonance frequency, intensity, and linewidth of the phonon mode, respectively. The dimensionless parameter q characterizes the spectral asymmetry and reflects the coupling strength between the phonon and the continuum of excitations. The black dashed lines in Fig. 3(f) show the fitted curves for each temperature, and the fitting parameters are summarized in Table 1.

Table 1. Fano-like response fit parameters at different temperatures. $\sigma_0, \gamma, \omega_0$, and q correspond to intensity, linewidth of the phonon mode, the resonance frequency, and the phonon–continuum coupling strength, respectively. The error bars of all fitting parameters are included.

T (K)	σ_0 ($\Omega^{-1}\cdot cm^{-1}$)	γ (cm^{-1})	ω_0 (cm^{-1})	q
10	294.83 (44.16)	3.66 (0.06)	137.73 (0.04)	–9.09 (0.67)
50	204.49 (31.42)	3.92 (0.06)	137.61 (0.04)	–10.46 (0.79)
100	150.36 (20.52)	4.36 (0.05)	137.02 (0.03)	–11.19 (0.75)
150	23.61 (5.18)	5.34 (0.05)	136.29 (0.03)	–24.12 (2.63)
200	11.41 (6.83)	6.17 (0.11)	135.93 (0.07)	–30.01 (8.96)
250	2.95 (1.13)	6.58 (0.04)	134.57 (0.03)	53.91 (10.38)
300	221.01 (42.29)	6.87 (0.19)	133.51 (0.12)	6.09 (0.60)
350	117.94 (13.40)	6.29 (0.06)	131.52 (0.04)	10.00 (0.57)

The phonon frequency ω_0 softens gradually from approximately 137.73 cm^{-1} at 10 K to 133.51 cm^{-1} at 300 K, followed by an abrupt shift down to 131.52 cm^{-1} at 350 K. This anomaly across T_N strongly suggests the presence of significant spin–phonon coupling. Below 250 K, the $|q|$ value increases with temperature while remaining significantly greater than 1. This trend suggests that the phonon line shape progressively approaches a symmetric Lorentzian profile, which is indicative of weak coupling between the phonon modes and the continuum background. At 300 K, however, the value of $|q|$ abruptly decreases to 6.09, indicating a pronounced change in the Fano asymmetry. As the temperature further increases up to 350 K, $|q|$ rises again. If the Fano line arises from interference between a phonon and the electronic continuum, $|q|$ would reflect the ratio of the corresponding matrix elements for exciting the phonon versus electronic excitations, as well as the electronic density of states at the phonon energy. However, across T_N, the primary changes in the band structure take place at least 0.475 eV below the Fermi level, far away from the phonon energy. In addition, the carrier density remains basically unchanged, indicating that electron–phonon coupling alone cannot explain the minimum in $|q|$. Given the evidence of strong spin–phonon coupling and the minimum $|q|$ near T_N, we thus conclude that the observed Fano line shape reflects interference between the phonon and a background of magnetic fluctuations, implying a modulation of the spin-exchange integral by lattice vibrations.

4. Conclusion

In summary, we have performed a detailed investigation of the charge dynamics in the altermagnetic semiconductor MnTe. The temperature-dependent resistivity exhibits a complex conduction mechanism, including impurity-related transport at low temperature, and enhanced scattering from phonons, magnons, and disordered spins above T_N. The optical conductivity reveals a suppressed Drude response, confirming the presence of itinerant carriers, which is consistent

with the p-type doping as indicated by previous ARPES measurements. Tauc analysis of the absorption edge identifies two distinct gaps, with an indirect gap of 0.475 eV attributed to impurity-assisted transitions and a direct gap of 1.60 eV at 10 K. Furthermore, a subtle differential feature observed near 1.44 eV in the optical conductivity above and below T_N might be linked to band splitting associated with the altermagnetic order. Additionally, the Fano asymmetry of the phonon mode near T_N reflects enhanced spin–phonon coupling and interference with magnetic fluctuations. These findings advance the fundamental understanding of MnTe and highlight the interplay between electronic, magnetic, and lattice degrees of freedom in this material.

Acknowledgements

R.Y.C. acknowledges the support by the National Key Research and Development Program of China (Grant Nos. 2021YFA1400400 and 2023YFA1406100), the National Natural Science Foundation of China (Grant No. 12074042), the Young Scientists Fund of the National Natural Science Foundation of China (Grant No. 11704033), and the Fundamental Research Funds for the Central Universities (Grant No. 2243300003). Y.F.G. acknowledges the open research fund of Beijing National Laboratory for Condensed Matter Physics (Grant No. 2023BNLCMPKF002). This work was supported by the Synergetic Extreme Condition User Facility (SECUF).

References

[1] Šmejkal L, Sinova J and Jungwirth T 2022 *Phys. Rev. X* **12** 040501
[2] Šmejkal L, Sinova J and Jungwirth T 2022 *Phys. Rev. X* **12** 031042
[3] Mazin I 2022 *Phys. Rev. X* **12** 040002
[4] Mazin I 2023 *Phys. Rev. B* **107** L100418
[5] Radaelli P G 2024 *Phys. Rev. B* **110** 214428
[6] McClarty P A and Rau J G 2024 *Phys. Rev. Lett.* **132** 176702
[7] Smolyanyuk A, Šmejkal L and Mazin I I 2025 *Phys. Rev. B* **111** 064406
[8] Parfenov O E, Averyanov D V, Sokolov I S, Mihalyuk A N, Kondratev O A, Taldenkov A N, Tokmachev A M and Storchak V G 2025 *J. Am. Chem. Soc.* **147** 5911
[9] Squire C F 1939 *Phys. Rev.* **56** 922
[10] Grazhdankina N and Gurfel D 1959 *Sov. Phys. J.* **35** 907
[11] Komatsubara T, Murakami M and Hirahara E 1963 *J. Phys. Soc. Jpn.* **18** 356
[12] Szuszkiewicz W, Hennion B, Witkowska B, Łusakowska E and Mycielski A 2005 *Phys. Status Solidi* **2** 1141
[13] Krause M and Bechstedt F 2013 *J. Supercond. Novel Magn.* **26** 1963
[14] Wang P, Zhu S C, Zou Y T, Chen H Y, Liu Y, Li W W, Chen J, Zhu J L, Wu L S, Wang S M, Yang W G, Xiao Y M, Chow P, Wang L P and Zhao Y S 2022 *Chem. Mater.* **34** 3931
[15] Chilcote M, Mazza A R, Lu Q, Gray I, Tian Q, Deng Q, Moseley D, Chen A H, Lapano J, Gardner J S, Eres G, Ward T Z, Feng E, Cao H, Lauter V, McGuire M A, Hermann R, Parker D, Han M G, Kayani A, Rimal G, Wu L, Charlton T R, Moore R G and Brahlek M 2024 *Adv. Funct. Mater.* **34** 2405829
[16] Lee S, Lee S, Jung S, Jung J, Kim D, Lee Y, Seok B, Kim J, Park B G, Šmejkal L, Kang C J and Kim C 2024 *Phys. Rev. Lett.* **132** 036702
[17] Kriegner D, Reichlova H, Grenzer J, Schmidt W, Ressouche E, Godinho J, Wagner T, Martin S Y, Shick A B, Volobuev V V, Springholz G, Holý V, Wunderlich J, Jungwirth T and Výborný K 2017 *Phys. Rev. B* **96** 214418
[18] Gonzalez Betancourt R D, Zubáč J, Gonzalez-Hernandez R, Geishendorf K, Šobáň Z, Springholz G, Olejník K, Šmejkal L, Sinova J, Jungwirth T, Goennenwein S T B, Thomas A, Reichlová H, Železný J and Kriegner D 2023 *Phys. Rev. Lett.* **130** 036702
[19] Zanmarchi G 1967 *J. Phys. Chem. Solids* **28** 2123
[20] Allen J, Lucovsky G and Mikkelsen J 1977 *Solid State Commun.* **24** 367
[21] Sandratskii L M, Egorov R F and Berdyshev A A 1981 *Phys. Status Solidi B* **104** 103
[22] Podgòrny M and Oleszkiewicz J 1983 *J. Phys. C: Solid State Phys.* **16** 2547
[23] Wei S H and Zunger A 1987 *Phys. Rev. B* **35** 2340
[24] Oleszkiewicz J, Kisiel A and Ignatowicz S 1988 *Thin Solid Films* **157** 1
[25] Angadi M and Thanigaimani V 1994 1994 *Phys. Status Solidi A* **143** K119
[26] Sato H, Mihara T, Furuta A, Tamura M, Mimura K, Happo N, Taniguchi M and Ueda Y 1997 *Phys. Rev. B* **56** 7222
[27] Ferrer-Roca C, Segura A, Reig C and Muñoz V 2000 *Phys. Rev. B* **61** 13679
[28] Reig C, Muñoz V, Gómez C, Ferrer C and Segura A 2001 *J. Cryst. Growth* **223** 349
[29] Tanner D B 2015 *Phys. Rev. B* **91** 035123
[30] Kluczyk K P, Gas K, Grzybowski M J, Skupiński P, Borysiewicz M A, Fas T, Suffczyński J, Domagala J Z, Grasza K, Mycielski A, Baj M, Ahn K H, Výborný K, Sawicki M and Gryglas-Borysiewicz M 2024 *Phys. Rev. B* **110** 155201
[31] Huang H, Qu T, Cheng Y, Tai L, Eckberg C, Pan Q, Alrasheed A, Chong S K, Dai B, Li Y, Shu Q, Yang C Y, Yu J X, Yin G and Wang K L 2024 (Preprint 2405.04686)
[32] Pereverzev Y V, Povstyanyi L V and Zvyagin A I 1976 *Sov. J. Low Temp. Phys.* **2** 311
[33] Efrem D'Sa J, Bhobe P, Priolkar K, Das A, Paranjpe S, Prabhu R and Sarode P 2005 *J. Magn. Magn. Mater.* **285** 267
[34] Chen Z G, Yuan R H, Dong T, Xu G, Shi Y G, Zheng P, Luo J L, Guo J G, Chen X L and Wang N L 2011 *Phys. Rev. B* **83** 220507
[35] Homes C C, Wang Z C, Fruhling K and Tafti F 2023 *Phys. Rev. B* **107** 045106
[36] Homes C, McConnell A, Clayman B, Bonn D, Liang R, Hardy W, Inoue M, Negishi H, Fournier P and Greene R 2000 *Phys. Rev. Lett.* **84** 5391
[37] Osumi T, Souma S, Aoyama T, Yamauchi K, Honma A, Nakayama K, Takahashi T, Ohgushi K and Sato T 2024 *Phys. Rev. B* **109** 115102
[38] Tauc J, Grigorovici R and Vancu A 1966 *Phys. Status Solidi B* **15** 627
[39] Okamura H, Michizawa T, Nanba T, Kimura S, Iga F and Takabatake T 2005 *J. Phys. Soc. Jpn.* **74** 1954
[40] Zhang J M, Lian R, Yang Y, Xu G, Zhong K and Huang Z 2017 *Sci. Rep.* **7** 43626
[41] Fano U 1961 *Phys. Rev.* **124** 1866
[42] Wenzel M, Ortiz B R, Wilson S D, Dressel M, Tsirlin A A and Uykur E 2022 *Phys. Rev. B* **105** 245123